ACS OMEGA

http://pubs.acs.org/journal/acsodf

Article

Novel Magnetic Fe_3O_4/α-FeOOH Nanocomposites and Their Enhanced Mechanism for Tetracycline Hydrochloride Removal in the Visible Photo-Fenton Process

Xinyi Huang, Hui Zhou, Xiaojun Yue, Songlin Ran, and Jianhua Zhu*

Cite This: *ACS Omega* 2021, 6, 9095−9103

Read Online

ACCESS | Metrics & More | Article Recommendations | Supporting Information

ABSTRACT: Magnetic Fe_3O_4/α-FeOOH heterojunction nanocomposites (denoted as Fe-NCs) have been synthesized by a fast one-pot hydrothermal method. The obtained Fe-NCs contain rich micropores with a high surface area of 135.15 m^2/g. The different phases in the composites can efficiently enhance the visible-light absorption, improving the separation and transfer of photogenerated electron−hole pairs during the photocatalytic reaction. Thus, they show excellent degradation and mineralization of tetracycline (TC) over a wide pH range (5−9) in the visible photo-Fenton reaction. Especially, the catalyst exhibits the highest adsorption capacity toward TC at a neutral pH, which facilitates the surface reactions of TC with active species. Experiments evidence that the high production of photogenerated holes and superoxide radicals ($O_2^{\bullet-}$) in Fe-NCs are favorable to the high catalytic efficiency. Combined with liquid chromatography−mass spectrometry, the possible pathway toward TC degradation was proposed.

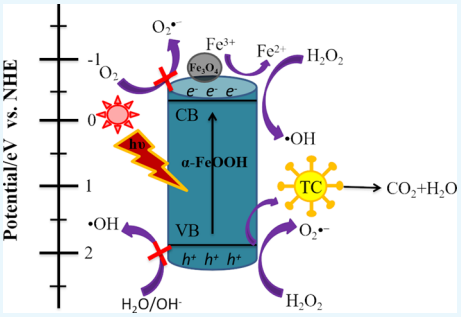

1. INTRODUCTION

Pharmaceutical antibiotics are considered as one of the most harmful pollutants in wastewater, which may cause serious impact on human living ecosystems.[1,2] Even small concentrations of antibiotics can lead to contamination of food and freshwater resources. Among different antibiotics, tetracycline (TC) has the second most production and usage as it has high antimicrobial activity against various pathogens.[3] Therefore, efficient removal of TC from wastewater, groundwater, and drinking water is of urgent importance for people's health. Until now, various methods have been designed, such as ozonation, physical adsorption, and microbial degradation, to efficiently eliminate this recalcitrant contaminant.[4−6] However, it is still difficult to completely degrade TC through traditional water treatment technologies.

Advanced oxidation processes, especially the Fenton oxidation technology, has been widely studied for wastewater treatment since it was first reported in 1894.[7] The reactive radicals including the hydroxyl radical (•OH) and superoxide radical ($O_2^{\bullet-}$) generated during the Fenton reaction could effectively decompose recalcitrant contaminants.[8] However, it still has many disadvantages, such as high operating cost, limited optimum pH range, and large volume of iron sludge produced.[9] To solve these problems, its derivative Fenton-like oxidation technology with the assistance of photo, ultrasonic, magnetic field, or other extra energy has been developed with enhanced degradation efficiency.[10−13] In particular, the photo-Fenton reaction is famous as some semiconductor catalysts can generate electron−hole pairs under light irradiation to enhance the production of reactive radicals and the catalytic efficiency.[14] The most important issue often focuses on improving the removal efficiency through efficient heterogeneous photo-Fenton catalysts. Moreover, in order to efficiently utilize solar energy in practical applications, a visible-light-assisted heterogeneous photo-Fenton catalyst is highly desired.[15]

Until now, many semiconductor materials have been reported to show high catalysis in the visible photo-Fenton system.[16−18] Especially, iron-based materials have been widely studied due to their excellent catalytic ability in the Fenton reaction.[19] Goethite (α-FeOOH) is an abundant and easily available mineral in nature, which has been widely studied for water treatment. However, pure α-FeOOH still has many limitations for photocatalysis, such as low photocatalytic activity and low electron−hole pair transfer rate.[20] Hence, appropriate modification approaches to solve this problem are necessary for practical applications. Combining α-FeOOH with other components to form binary nanocomposites has been proved to be a very effective way. Recently, many α-FeOOH-based nanocomposites, such as carbon quantum dots/α-FeOOH, g-C_3N_4/α-FeOOH, and γ-Fe_2O_3/α-FeOOH,

Received: January 12, 2021
Accepted: February 23, 2021
Published: March 26, 2021

have been designed.[21−23] They usually showed better visible-light absorption intensity or accelerated electron transfer, facilitating the recycling of the catalyst. However, there still exists a huge challenge to explore the appropriate nanocomposite structures for α-FeOOH-based photocatalysts in light of different application scenarios.

In this work, magnetic Fe_3O_4/α-FeOOH heterojunction nanocomposite catalysts (Fe-NCs) composed of α-FeOOH nanorods decorated with Fe_3O_4 nanoparticles (NPs) have been successfully synthesized via a facile one-pot hydrothermal method. The hybrid nanocomposites show significantly enhanced visible-light absorption of the catalyst and accelerated charge separation and transfer owing to the interaction between α-FeOOH and Fe_3O_4, which in turn promotes the high production of superoxide radicals ($O_2^{\bullet-}$). They exhibit excellent visible photo-Fenton performance for the degradation of TC over a wide pH range of 5−9. Further, the probable catalytic mechanism for H_2O_2 activation and the pathway for TC degradation in the visible photo-Fenton reaction were proposed.

2. RESULTS AND DISCUSSION

2.1. Characterization of Catalysts. Well-defined nanorods (~200 in length) decorated with many small cubic NPs (~10 nm in size) were synthesized via a fast one-pot hydrothermal process (Figures 1a, S1, and S2). The X-ray diffraction (XRD) pattern (Figure 1c) reveals two phases of α-FeOOH (JCPDS no. 29-0731) and Fe_3O_4 (JCPDS no. 75-1372). The high-resolution transmission electron microscopy (HRTEM) images show two lattice fringes of 0.269 nm in nanorods and 0.302 nm in NPs, which are in agreement with the lattice planes (130) of goethite and (220) of magnetite (Figure 1b), respectively. No individual α-FeOOH nanorods or Fe_3O_4 NPs were observed even after the ultrasonic treatment, indicating the stable attachment of Fe_3O_4 NPs onto the α-FeOOH nanorods.

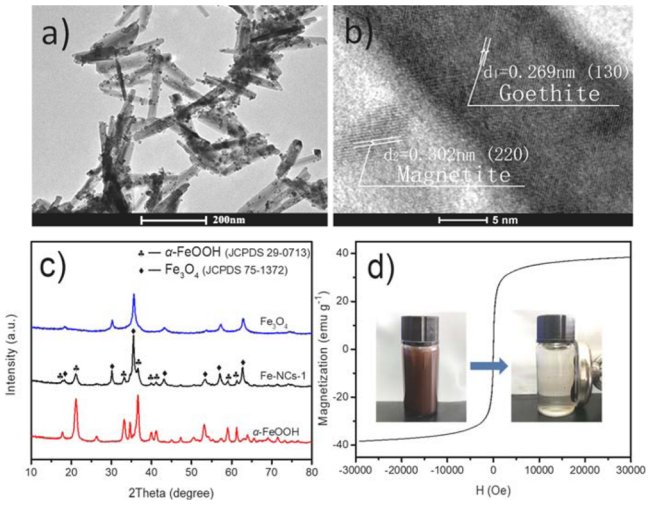

Figure 1. Characterization of prepared Fe-NCs-1. (a) TEM image; (b) corresponding HRTEM images; (c) XRD patterns of different samples; and (d) M−S curve (insets are the corresponding magnetic properties in the presence of an external magnetic field).

Interestingly, the ratios of two phases could be adjusted by the addition of a different amount of N_2H_4 (Figure S3). The more N_2H_4 was introduced into the reaction system, the higher the percentage of the Fe_3O_4 phase could be obtained in the resultant nanocomposites, which was further confirmed by scanning electron microscopy (SEM) and TEM images (Figures S1 and S2). Fe-NCs-1 show a M_s value of 38.6 emu g^{-1} at 15 kOe (Figure 1d) with an obvious hysteresis loop, which further confirmed the existence of magnetite. The magnetic properties indicate that they can be easily separated from the treated wastewater in the presence of an external magnetic field (inset of Figure 1d). For contrast experiments, pure α-FeOOH nanorods and Fe_3O_4 NPs were synthesized (Figures 1c, S4).

The UV−vis diffuse reflectance spectra (DRS) of pure α-FeOOH nanorods only display an obvious absorption between 230 and 500 nm (Figure 2a), which may limit the potential application in photocatalysis owing to the low utilization efficiency of the visible light. By contrast, the as-prepared Fe-NCs-1 samples show enhanced adsorption in the UV and visible-light range, higher than both pure Fe_3O_4 and α-FeOOH. Thus, the visible-light utilization efficiency of α-FeOOH is significantly enhanced by modifying Fe_3O_4 NPs, which may lead to better photocatalytic ability under visible-light irradiation.

Nitrogen adsorption−desorption isotherms of Fe-NCs were obtained to determine the specific surface areas and pore size distribution (Figures 2b, S5). Fe-NCs-1 exhibit the highest specific area reached, 135.15 m^2/g, and the N_2 adsorption−desorption isotherms are typical type-IV isotherms with visible hysteresis loops, indicating the existence of mesopores. The average pore size analyzed by the Barrett−Joyner−Halenda method shows that both micropores and mesopores are in the presence of nanocomposites (inset in Figure 2b). The zeta potential variation of Fe-NC-1 suspensions under different pH values is depicted in Figure S6, and the point of zero charge is 3.8.

The charge transfer and conductivity of as-prepared nanocomposites were measured by electrochemical impedance spectra (Figure 2c) as they were closely linked with heterogeneous photocatalytic activity.[24] The smaller diameter of the semicircle means that semiconductor materials possess better conductivity and more effective charge carrier migration with less resistance and a lower recombination rate of electron−hole pairs.[25] As expected, Fe-NCs-1 displayed the smallest semicircle diameter, indicating that the combination of Fe_3O_4 with α-FeOOH has effectively improved the conductivity, accelerating the charge transfer and reducing the recombination rate of photogenerated electron−hole pairs. The photocurrent response spectra of Fe_3O_4, α-FeOOH, and Fe-NCs-1 were also measured (Figure 2d). The photoresponse ability of Fe-NCs-1 is higher than that of both Fe_3O_4 and α-FeOOH. This indicates that the separation and transfer efficiency of photogenerated electron−hole pairs increases greatly. Evidently, the combination of Fe_3O_4 and α-FeOOH has effectively accelerated the electron transfer and reduced the recombination of electron−hole pairs.

2.2. Degradation of Organic Pollutants. The catalytic activities of Fe-NCs were evaluated by TC degradation under various conditions. Fe-NCs-1 were selected as the model catalyst as they showed the highest catalytic efficiency in visible photo-Fenton degradation (Figure S7). Under the single influencing factor of visible light or H_2O_2, about 35 and 65% of TC was removed after 90 min (Figure 3a), respectively. When visible light and H_2O_2 were applied together, the degradation rate increased markedly to 96%, indicating that they had

https://doi.org/10.1021/acsomega.1c00204
ACS Omega 2021, 6, 9095−9103

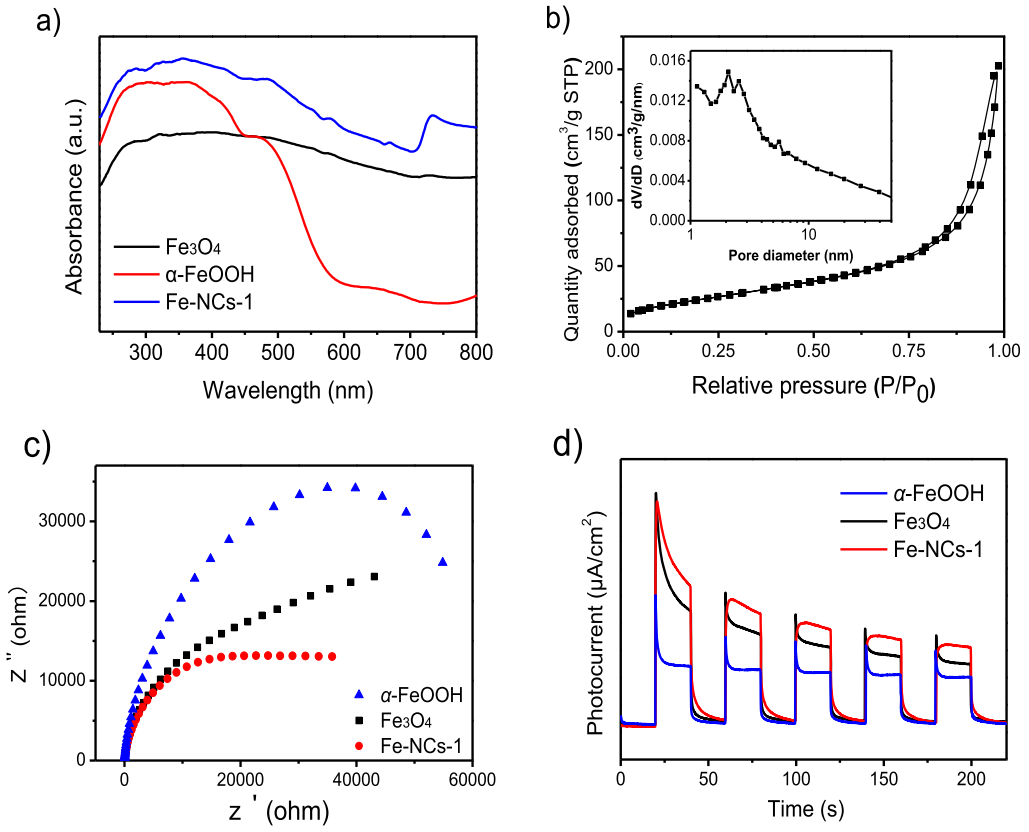

Figure 2. Physical and chemical properties of Fe-NCs-1. (a) UV−vis DRS spectra; (b) N_2 adsorption−desorption isotherms curves. The inset is the corresponding pore diameter distribution; (c) EIS Nyquist plots; and (d) photocurrent spectra.

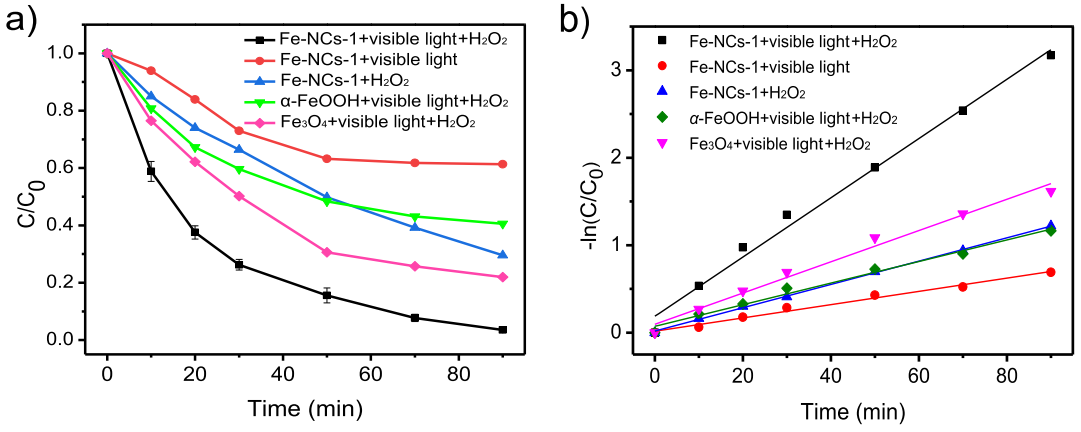

Figure 3. (a) Photocatalytic degradation of TC in different systems and (b) corresponding first-order plots (catalyst loading = 0.5 g·L^{-1}; [H_2O_2] = 10 mM; [TC] = 10 mg·L^{-1}; pH = 5; and T = 25 °C).

synergistic catalytic effects on the TC degradation. To prove the synergistic action between α-FeOOH and Fe_3O_4, the degradation rates of pure α-FeOOH and Fe_3O_4 were also investigated. The corresponding degradation efficiencies are only 55 and 78% under the combined condition of visible light and H_2O_2. This manifests that α-FeOOH and Fe_3O_4 in Fe-NCs-1 produce not a simple catalytic effect superposition but a synergistic effect.

TC degradation by Fe-NCs-1 is followed by pseudo-first-order kinetics (Figure 3b), and the reaction constants for Fe_3O_4, α-FeOOH, and Fe_3O_4@α-FeOOH are calculated to be 1.07, 0.74, and 2.03 h^{-1}, respectively. Further, the degradation curves indicate that the Fenton process (blue curve in Figure 3b) contributes more to TC degradation than the photocatalytic process does (red curve in Figure 3b) as their corresponding constants are 0.80 and 0.46 h^{-1}, respectively.

The optimal catalytic condition in the visible photo-Fenton systems was explored. The degradation efficiency increases with the amount of catalyst dosage (0.1−0.75 g L^{-1}) (Figure 4a). At a concentration of the catalyst of 75 mg, the degradation efficiency can even reach 100% after 90 min. Evidently, the sufficient amount of the catalyst can provide enough active sites for activated species generation, which further enhances the catalytic efficiency. Hence, 75 mg Fe-NCs-1 is the optimum amount for the photo-Fenton degradation of TC.

https://doi.org/10.1021/acsomega.1c00204
ACS Omega 2021, 6, 9095−9103

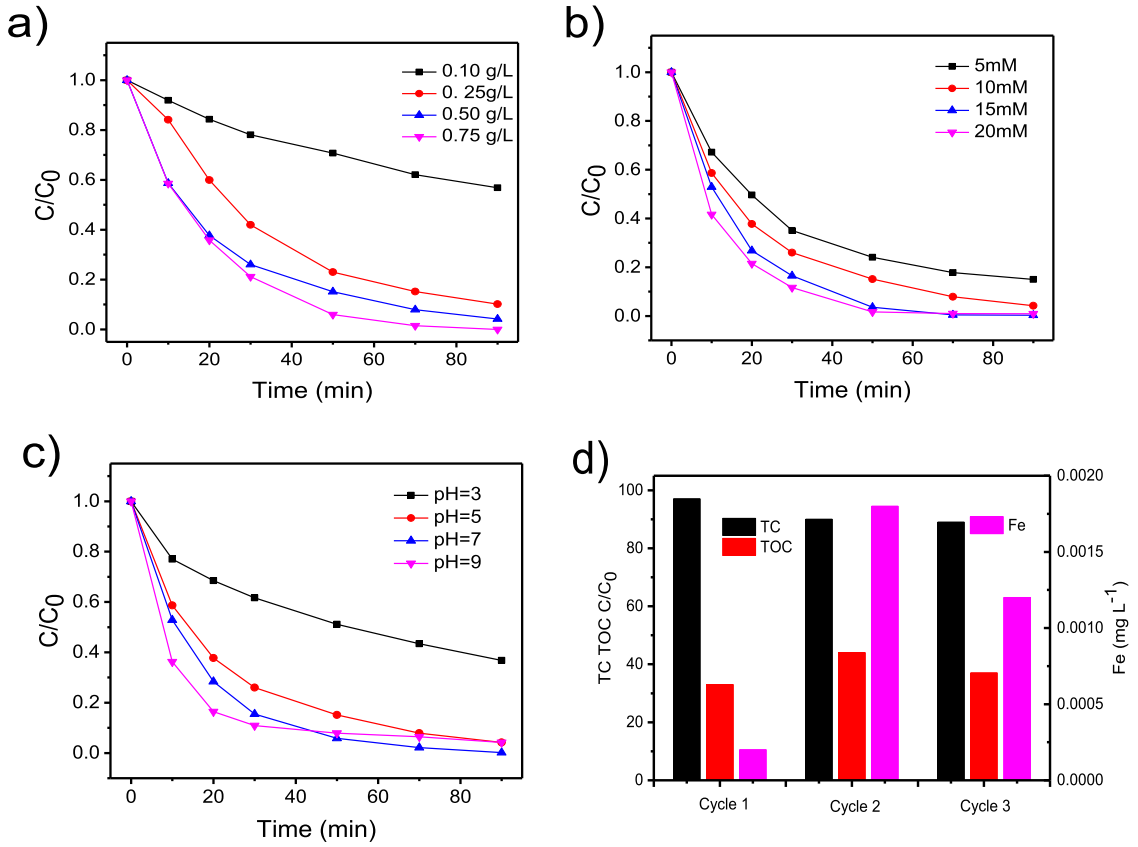

Figure 4. Effects of (a) catalyst dosage, (b) H_2O_2 dosage, and (c) initial pH on the catalytic degradation process. (d) TC degradation, TOC removal, and leaching ions in multi-cycle batch experiments.

With the increasing H_2O_2 concentrations, the degradation efficiency also increased gradually, and TC could be completely degraded at a concentration of 15 mM (Figure 4b). Further increased H_2O_2 dosage to 20 mM showed no obvious enhancement. As H_2O_2 with high dosage may result in unnecessary scavenging of free radicals ($^{\bullet}OH$, $O_2^{\bullet-}$), the optimal concentration of H_2O_2 is about 10 mM to achieve the best utilization of active radicals.

The initial pH values (pH_0) can influence the adsorption between the catalyst and contaminant in chemical oxidation processes, which may further affect the degradation efficiency.[26] Experiments revealed that Fe-NCs-1 exhibited high catalysis captivity toward TC between pH = 5 and 9 (Figure 4c), and the degradation efficiencies were all above 95%. Especially, under the neutral condition, the degradation efficiency of TC could reach 100%. By contrast, the lowest degradation efficiency (63%) was obtained at pH = 3 within 90 min. This is contrary to some reports that α-FeOOH as the Fenton catalyst has high catalytic activity only at low pH ranges and shows a significant decrease in neutral or even alkaline conditions.[27] The underlying reason may relate closely with the low adsorption capacity and low iron leaching at a low pH value.

In the solution, TC has three ion forms: the protonated form (TCH_3^+, pH < 3.3), monoanionic form (TC^-, pH > 7.7), and neutral form (TCH_2^0, pH = 3.3−7.7). At pH_0 = 3, the zeta potential of the catalyst surface was positive, which shows electrostatic repulsion with TCH_3^+. Hence, Fe-NCs-1 show the lowest absorption capacity of about 18% (Figure S8). As most active radicals are generated on the catalyst surface, low absorption will stymie the reaction between TC and active radicals, leading to the low degradation efficiency. Simultaneously, to confirm that the primary reactions are heterogeneous reactions occurring on the surface of the catalyst rather than homogeneous reactions occurring in the solution, iron leaching at different pH_0 values was investigated. As shown in Figure S8, the catalyst shows good stability over a wide pH range, while it showed the highest ion leaching at pH = 3 (0.028 mg L^{-1}) due to the enhanced Fenton reactions in the acid solution. However, iron leaching under the acid condition in this research is stilled much lower than that in other homogeneous Fenton systems.[28] Although some reports demonstrated that a low pH favored the pollutant degradation, they often had close relationship with high iron leaching, which would promote the homogeneous reaction in the solution.

The recycling capacity and stability of catalysts were evaluated for practical applications. As shown in Figure 4d, the degradation ability of Fe-NCs-1 decreases gradually after each cycle, but they still maintain a 90% degradation rate after three cycles. The efficiency of TC mineralization after each recycling run was also measured by testing solution total organic carbon (TOC). About 35% of TOC can be removed after each photo-Fenton reaction, which means a portion of TC converted to CO_2. The concentrations of released iron ions were characterized by inductively coupled plasma−optical emission spectroscopy (ICP−OES) after different numbers of recycling cycles. The leaching iron concentration shows significant increase in the second and third cycles but is still lower than 0.002 mg L^{-1}. Hence, its environmental impact can be ignored as the environmentally friendly property of iron ions.

https://doi.org/10.1021/acsomega.1c00204
ACS Omega 2021, 6, 9095−9103

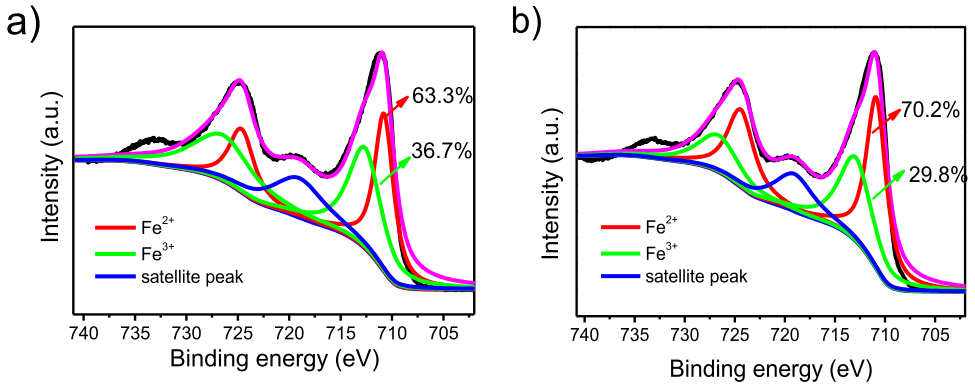

Figure 5. XPS spectra of Fe-NCs-1. (a) Fe 2p before catalysis and (b) after catalysis.

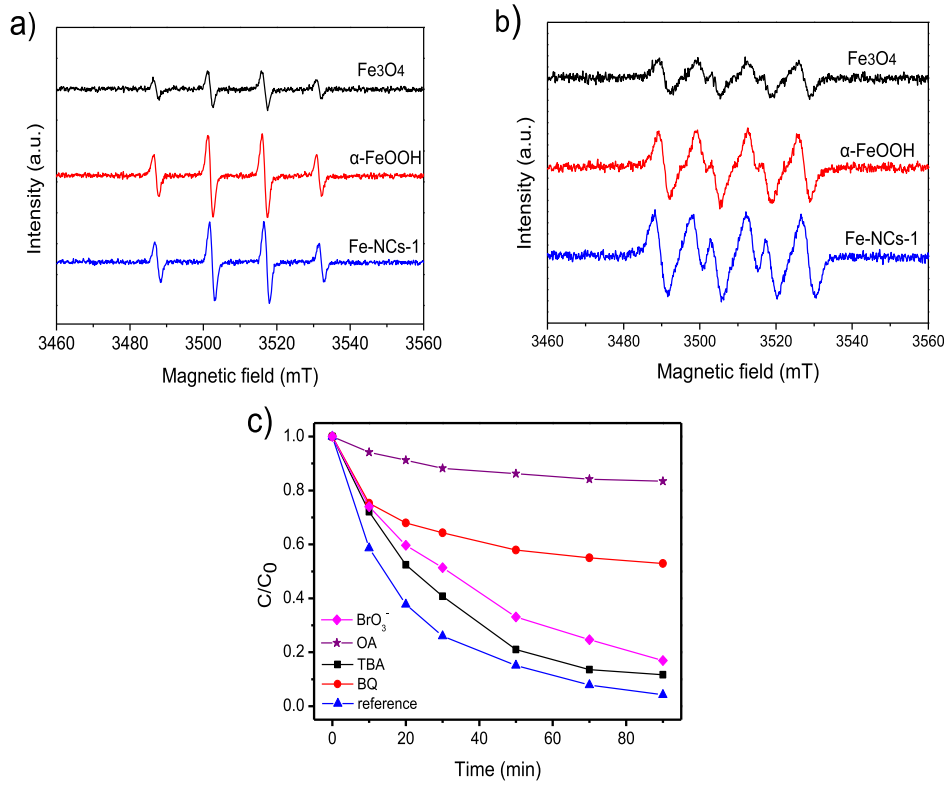

Figure 6. EPR spectra for DMPO adducts in Fe-NCs-1/visible photo-Fenton systems. (a) DMPO−$^{\bullet}$OH; (b) DMPO−$O_2^{\bullet-}$; and (c) radical scavenger quenching test for TC degradation in the visible photo-Fenton reaction.

2.3. Degradation Mechanism. The surface metals species of Fe-NCs-1 before and after the catalytic reaction were characterized by X-ray photoelectron spectroscopy (XPS) analysis. Fe^{2+} and Fe^{3+} peaks are identified at 710.8 and 724.7 eV for Fe^{2+} and at 712.9 and 727.03 eV for Fe^{3+}, with a satellite Fe $2p_{3/2}$ peak at 719.4 eV (Figure 5a). These results are consistent with the XRD analysis that α-FeOOH and Fe_3O_4 coexist in the nanocomposites. The content of Fe^{2+} and Fe^{3+} in catalysts was evaluated by their peak area. The content of Fe^{2+} (Figure 5b) increases from 63.3% (before catalysis) to 70.2% (after catalysis). This can be attributed to the reaction of Fe^{3+} with photogenerated electrons producing Fe^{2+} in the solution, which will further react with H_2O_2 to produce $^{\bullet}$OH radicals.

To elucidate the transfer process of electron−hole pairs in the Fe-NCs/photo-Fenton system, it is necessary to determine the energy band positions of catalysts. Under the irradiation of visible light, the electrons of α-FeOOH and Fe_3O_4 are excited from the valence band (VB) to the conduction band (CB) with the generation of photogenerated electron−hole pairs. The specific band gap (E_g) of as-obtained samples was extracted by plotting $(\alpha h\nu)^2$ versus $h\nu$ (Figure S9a), and the E_g of α-FeOOH, Fe_3O_4, and Fe-NCs-1 were +1.88, +0.8, and +1.27 eV, respectively. The lower band gap energies of Fe-NCs-1 than that of pure α-FeOOH are mainly attributed to the interaction between Fe_3O_4 and α-FeOOH at the micro-scale length. As a result, the production of charge carriers was remarkably improved under the same visible light irradiation, leading to the significant enhancement of photocatalytic activity.[29]

Mott−Schottky plots were also tested to explore the flat potential (Figure S9b). Three samples were typical n-type semiconductors as they all have a negative slope of the tangent.[30] The E_{CB} positions of α-FeOOH, Fe_3O_4, and Fe-NCs-1 were calculated as −0.27, −0.31, and −0.2 eV versus

https://doi.org/10.1021/acsomega.1c00204
ACS Omega 2021, 6, 9095−9103

normal hydrogen electrode (NHE), respectively. In this circumstance, the electrons on the CB can react with H_2O_2 to produce $^{\bullet}OH$ but cannot react with adsorbed oxygen to yield $O_2^{\bullet-}$ radicals.[31] As $E_{VB} = E_{CB} + E_g$, the E_{VB} of α-FeOOH, Fe_3O_4, and Fe-NCs-1 were calculated to be about +1.61, +0.49, and +1.07 eV versus NHE, respectively. Because the E_{VB} of α-FeOOH is higher than that of $H_2O_2/O_2^{\bullet-}$ (+0.68 eV vs NHE), the h^+ on the VB can promote the production of $O_2^{\bullet-}$. However, the h^+ on the VB of α-FeOOH was much more negative than the standard redox potential of $^{\bullet}OH/OH^-$ and $^{\bullet}OH/H_2O$ (+1.99 and +2.27 eV vs NHE, respectively), the photogenerated holes cannot react with OH^- groups and H_2O molecules to yield $^{\bullet}OH$ radicals.

EPR characterization employing spin trap DMPO was carried out to identify free radicals generated in the TC degradation process. The quantitative information was provided by the intensity of DMPO radical adduct signals. Consistent with the energy band calculation results, both the signals of $^{\bullet}OH$ and $O_2^{\bullet-}$ have been detected in Fe-NCs-1. As shown in Figure 6a, the fourfold characteristic peaks of DMPO−$^{\bullet}OH$ adducts with an intensity ratio of 1:2:2:1 are distinguishable, which is corresponding to the appearance of $^{\bullet}OH$ in three different systems.[32] The intensities of DMPO−$^{\bullet}OH$ signals produced in α-FeOOH and Fe-NCs-1 systems are almost the same but much higher than those in Fe_3O_4 systems. That means that α-FeOOH and Fe-NCs-1 are more favorable for the production of $^{\bullet}OH$ in the photo-Fenton system. Further, the intensities of DMPO−$O_2^{\bullet-}$ signals in the Fe-NCs-1 visible photo-Fenton system is the highest among three catalysts (Figure 6b), which implies that the composites are most beneficial to the generation of $O_2^{\bullet-}$.

Scavenger quenching tests were also conducted to ascertain the importance of different radicals for TC degradation (Figure 6c). Tertiary butanol (TBA) was applied to quench $^{\bullet}OH$ as it has high reactivity toward $^{\bullet}OH$ ($k_{OH\bullet}$ = 3.8 to 7.6 × 10^8 M^{-1} s^{-1}). After addition of TBA, the TC removal speed became slower, and the degradation rate dropped to 89% within 90 min compared with that in the reference. This means that although the $^{\bullet}OH$ radical shows a sight effect on the TC degradation, it may have a synergistic effect with other activated radicals. 1,4-Benzoquinone, a scavenger for $O_2^{\bullet-}$ radicals, showed an obvious inhibitory effect on TC degradation. After the addition, the TC degradation efficiency decreased drastically to 47%, indicating that $O_2^{\bullet-}$ played an important role in the destruction of TC in the visible photo-Fenton system.

Photogenerated electrons and holes generated in the photocatalytic process may also contribute much to the production of active radicals and pollutant degradation. The addition of BrO_3^-, a scavenger for photogenerated electrons, shows a slight inhibitory effect for TC degradation. This indicates that the electrons on the CB cannot promote the production of active radicals for organic degradation, although it may accelerate the cycle of Fe^{3+}/Fe^{2+} for the homogeneous Fenton reaction. Thus, photogenerated electrons are not the key factors in the catalytic process.

Besides, ammonium oxalate was added as a scavenger of photogenerated holes, which reveals significantly inhibitory effects on the TC degradation (17%). Photogenerated holes can degrade TC directly and react with H_2O_2 to produce $O_2^{\bullet-}$, according to the calculated energy band positions. Combined with the results of scavenger quenching tests, both photogenerated holes and $O_2^{\bullet-}$ contributed much to the TC degradation.

Other factors are also favorable to TC degradation, for example, adsorption. As superoxide radicals have a short lifetime of less than 1 μs and holes generate on the catalyst surface, they tend to attack the TC molecules on the surface of the catalyst. Therefore, the high adsorption capacity of the catalyst toward TC is beneficial to hole and $O_2^{\bullet-}$ attack and subsequent degradation of TC molecules.

According to the aforementioned analysis, a possible photocatalytic mechanism of TC degradation is elucidated in Figure 7. Initially, the organic pollutant TC is adsorbed onto

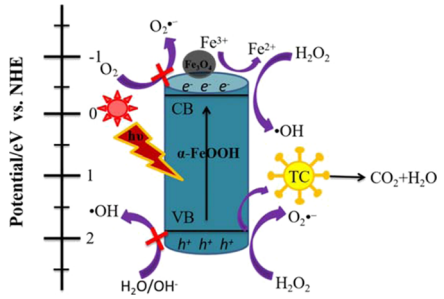

Figure 7. Possible catalytic mechanisms for visible photo-Fenton degradation of TC by Fe-NCs-1.

the surface of Fe-NCs via electrostatic interaction and chemical bonds. Then, under the irradiation of visible light, the electrons in the VB of α-FeOOH nanorods are excited and move to the CB with the generation of photogenerated holes in the VB (eq 1). The Fe_3O_4 NPs in the nanocomposites can effectively promote the separation of electrons and holes based on the results of electrochemical tests. The generated holes can directly destruct the adsorbed TC molecules on the surface of the catalyst or motivate H_2O_2 to produce the activated radicals of $O_2^{\bullet-}$ (eq 3). Meanwhile, the photogenerated electrons can stimulate the production of $^{\bullet}OH$ via the reaction of (eq 2) and circulation of Fe^{3+} and Fe^{2+} (eqs 4 and 6). The produced Fe^{2+} can react with H_2O_2 to generate $^{\bullet}OH$ (eq 5), and α-FeOOH and Fe_3O_4 can react with H_2O_2 directly to produce $^{\bullet}OH$ through the Fenton process. Finally, radical species ($O_2^{\bullet-}$ and $^{\bullet}OH$) and h^+ can effectively attack the C−C double bond in TC molecules to produce degradation intermediates, which subsequently convert into CO_2 and H_2O. The main reactions are summarized as follows

$$\alpha\text{-FeOOH/Fe}_3\text{O}_4 + h\nu \rightarrow \text{Fe}_3\text{O}_4/\alpha\text{-FeOOH/}(e^- + h^+) \quad (1)$$

$$H_2O_2 + e^- \rightarrow 2^{\bullet}OH \quad (2)$$

$$H_2O_2 + h^+ \rightarrow O_2^{\bullet-} + H_2O \quad (3)$$

$$Fe^{3+} + e^- \rightarrow Fe^{2+} \quad (4)$$

$$Fe^{2+} + H_2O_2 \rightarrow Fe^{3+} + {}^{\bullet}OH + OH^- \quad (5)$$

$$Fe^{3+} + e^- \rightarrow \text{circulation} \quad (6)$$

2.4. TC Degradation Intermediates and Biotoxicity. The intermediates formed during the visible photo-Fenton process were further investigated through the liquid chromatography−mass spectrometry (LC−MS) analysis (Figure S10). According to the results of LC−MS, the possible

https://doi.org/10.1021/acsomega.1c00204
ACS Omega 2021, 6, 9095−9103

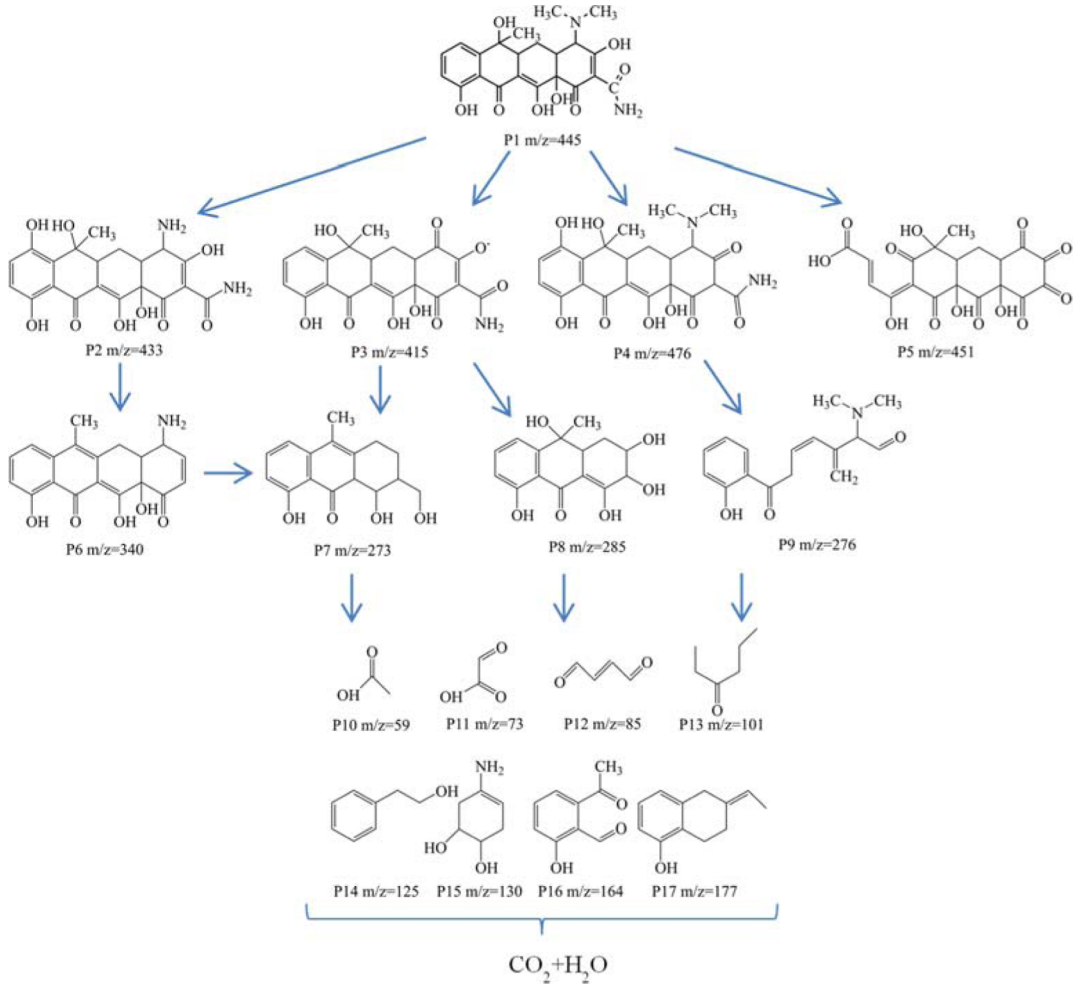

Figure 8. Possible degradation pathway of TC toward the Fe-NCs-1 under the visible photo-Fenton process.

degradation pathway and molecular structures of intermediates are presented in Figure 8. The peak with a m/z of 445 is designated to the TC molecule. After being attacked by active free radicals, the different intermediates P2, P3, and P4 were developed from the deamination, demethylation, and hydroxylation process of TC, respectively. The intermediate products of P5 were developed from a more complex way.[33] As $O_2^{\bullet-}$ can destroy the aromatic ring and amino group of TC, the intermediates of P6, P7, P8, and P9 are formed through the ring opening reactions and the cleavage of the carbon bond.[34] Finally, the intermediates undergo further oxidation into smaller molecule products P10−P17 with a short chain and are ultimately changed into carbon dioxide and water. The complex intermediate process illuminated why TC has a lower TOC removal efficiency.

3. CONCLUSIONS

Briefly, Fe_3O_4/α-FeOOH nanocomposites have been synthesized via a facile hydrothermal method. The composites showed stronger visible-light harvest than pure Fe_3O_4 and α-FeOOH. They exhibited a high specific area with rich micropores and better electrochemistry performance, favorable for excellent catalytic degradation of TC in the visible photo-Fenton process. EPR tests showed that the $O_2^{\bullet-}$ produced during the catalytic process was enhanced, which was responsible for the excellent degradation ability, according to the radical scavenger quenching test. Further, the reasons for more superoxide radicals produced in the Fe_3O_4/α-FeOOH were furnished. This work gives new insights into the mechanism of heterojunction nanocomposite catalysts applied in environmental remediation.

4. EXPERIMENTAL SECTION

4.1. Materials. Iron(III) nitrate nonahydrate, hydrazine hydrate, and ethyl alcohol were purchased from Shanghai Sinopharm Chemical Reagent Co., Ltd. Hexamethylenetetramine (HMT) and TC was purchased from Sigma Industrial Corporation. All aqueous solutions were prepared using ultrapure water (18.2 MΩ cm) from the water purifier (Elga PURE-LAB Chorus). All materials were used as received without further purification.

4.2. Preparation of Catalysts. The Fe-NCs were synthesized by a simple one-pot hydrothermal method. Typically, 0.404 g $Fe(NO_3)_3{\cdot}9H_2O$ was dissolved in 35 mL of ultrapure water, and 0.701 g HMT was added to obtain a crimson solution. Then, a desired amount of $N_2H_4{\cdot}H_2O$ was poured into the solution under vigorously magnetic stirring for 30 min. The mixed solution was then added to a Teflon-lined stainless container. After the hydrothermal process at 80 °C for 1 h, black precipitates were centrifuged at 8000 rpm. All products were washed with deionized water and absolute alcohol three times and dried at 60 °C overnight. Fe-NCs

https://doi.org/10.1021/acsomega.1c00204
ACS Omega 2021, 6, 9095−9103

obtained by adding 0.5, 1, and 3 mL $N_2H_4{\cdot}H_2O$ were denoted as Fe-NCs-0.5, Fe-NCs-1, and Fe-NCs-3, respectively. The synthesis protocol of α-FeOOH nanorods follows the Fe-CNs without the addition of HMT. The synthesis of Fe_3O_4 NPs follows that of Fe-CNs, except that 1 M NaOH was used to adjust the pH to 4.7 rather than HMT.

4.3. Catalytic Experiments in the Visible Photo-Fenton System. The TC degradation via the visible photo-Fenton reaction was carried out in a 200 mL glass vessel, and a 300 W Xe lamp (PLS-SXE300c, $\lambda \geq 420$ nm) was placed above it. This reaction was maintained at room temperature by circulating water. In a typical experiment, the suspension containing 0.5 g L^{-1} catalyst and 10 mg L^{-1} TC was magnetically stirred in dark for 30 min to reach the adsorption−desorption equilibrium, and then, the concentration of TC was detected to calculate the adsorption efficiency. The visible photo-Fenton reaction was started by adding 0.1 mL of H_2O_2 (10 mM) and turning on the lamp. The initial pH values were adjusted by H_2SO_4 and NaOH. The samples at different reaction times were withdrawn and filtered through a Millipore filter (0.25 μm) for analysis. The TC concentrations were determined by a UV−vis spectrometer. For the reusability experiments, the catalyst was separated by an external magnet and washed by distilled water three times and dried at 60 °C overnight.

4.4. Characterization. X-ray powder diffraction patterns were obtained on a Rigaku SmartLab X-ray diffractometer equipped with graphite monochromatized Cu Kα radiation (λ = 1.54178 Å). The morphology of products was observed by using a Hitachi S-4800 field emission scanning electron microscope. High-resolution transmission electron microscope photographs were obtained on a JEOL JEM-2011 microscope at an accelerating voltage of 200 kV. The Brunauer−Emmett−Teller (BET) surface area of samples was determined from BET measurements using a TriStarII 3020 M surface area and porosity analyzer. The magnetic properties of the sample were characterized using a vibrating sample magnetometer and a Quantum Design PPMS-9 physical property measurement system. Electrochemical impedance spectroscopy (EIS) was carried out on an electrochemical workstation (CHI66E) with the as-prepared FTO glass samples, a piece of Pt, and a Hg/$HgCl_2$ electrode (saturated calomel electrode and saturated KCl) as the working electrode, counter electrode, and reference electrode, respectively. Photocurrent measurements were taken in a typical three-electrode configuration. 0.5 mol/L Na_2SO_4 was used as the electrolyte solution. A 300 W Xe arc lamp (PLS-SXE300) was used as the light source, and the periodic ON/OFF photocurrent response was measured at a definite time interval. The N_2 adsorption−desorption isotherm was obtained using an accelerated surface area and porosimetry system (Autosorb-iQ, Quantachrome). UV−visible DRS were recorded on a Hitachi UV3600 spectrophotometer. The surface charge property of the samples in aqueous solution was measured by a Malvern 3000 Zetasizer. XPS spectra were recorded using an ESCALAB 250 Xi spectrometer (Thermo Fisher Scientific) fitted with an Al Kα radiation source. The ICP−OES was measured by Agilent 730. The TC concentrations were measured by a UV−vis spectrometer (Analytik Jena, SPECORD200 PLUS). The electron spin resonance (ESR) investigations were conducted with a Bruker A300 ESR spectrometer. LC−MS analysis was carried out with a liquid chromatograph coupled to a mass spectrometer (Q Exactive Plus LCMS, Thermo Scientific).

■ ASSOCIATED CONTENT

Supporting Information

The Supporting Information is available free of charge at https://pubs.acs.org/doi/10.1021/acsomega.1c00204.

SEM and TEM images, XRD, BET, zeta potential, LC−MS patterns, catalytic efficiency, optical property curves, adsorption, and ion leaching histogram of samples (PDF)

■ AUTHOR INFORMATION

Corresponding Author

Jianhua Zhu − *Anhui Province Key Laboratory of Metallurgical Emission Reduction and Resources & Metallurgical Reduction and Comprehensive Utilization of Resources of Key Laboratory (Ministry of Education), Anhui University of Technology, Maanshan 243002, Anhui, P. R. China;* orcid.org/0000-0002-0937-8873; Email: zjianhua@ahut.edu.cn

Authors

Xinyi Huang − *Anhui Province Key Laboratory of Metallurgical Emission Reduction, Anhui University of Technology, Maanshan 243002, Anhui, P. R. China;* orcid.org/0000-0001-9716-9547

Hui Zhou − *Anhui Province Key Laboratory of Metallurgical Emission Reduction, Anhui University of Technology, Maanshan 243002, Anhui, P. R. China*

Xiaojun Yue − *Anhui Province Key Laboratory of Metallurgical Emission Reduction, Anhui University of Technology, Maanshan 243002, Anhui, P. R. China*

Songlin Ran − *Anhui Province Key Laboratory of Metallurgical Emission Reduction, Anhui University of Technology, Maanshan 243002, Anhui, P. R. China*

Complete contact information is available at: https://pubs.acs.org/10.1021/acsomega.1c00204

Author Contributions

X.H. performed the sample synthesis, took the pictures of SEM and TEM, performed data analysis, and wrote the preliminary manuscript. J. Z. conceived the project idea and designed the experimental work, conceptualized the research, edited the manuscript, and led the overall research work. H.Z. and X.Y. supported the experimental methodology and characterization setups. S.R. contributed to the formal data analyses and scientific discussion of the results. All authors contributed to the writing, reviewing, and editing of the final manuscript.

Notes

The authors declare no competing financial interest.

■ ACKNOWLEDGMENTS

The authors thank the Natural Science Foundation of the Anhui Higher Education Institutions of China (KJ2020A0256), the University Collaborative Innovation Project in Anhui Province (GXXT-2019-15, GXXT-2020-07), and the National Natural Science Foundation of China (21571004).

■ REFERENCES

(1) Zhao, R.; Sun, X.; Jin, Y.; Han, J.; Wang, L.; Liu, F. Au/Pd/g-C_3N_4 nanocomposites for photocatalytic degradation of tetracycline hydrochloride. *J. Mater. Sci.* **2019**, *54*, 5445−5456.

(2) Cao, J.; Xiong, Z.; Lai, B. Effect of initial pH on the tetracycline (TC) removal by zero-valent iron: Adsorption, oxidation and reduction. *Chem. Eng. J.* **2018**, *343*, 492−499.
(3) Daghrir, R.; Drogui, P. Tetracycline antibiotics in the environment: a review. *Environ. Chem. Lett.* **2013**, *11*, 209−227.
(4) Lv, A.; Hu, C.; Nie, Y.; Qu, J. Catalytic ozonation of toxic pollutants over magnetic cobalt and manganese co-doped γ-Fe_2O_3. *Appl. Catal., B* **2010**, *100*, 62−67.
(5) Zhu, J.; Shu, J.; Yue, X.; Su, Y. Hollow and porous octacalcium phosphate superstructures mediated by the polyelectrolyte PSS: a superior removal capacity for heavy metal and antibiotics. *J. Mater. Sci.* **2020**, *55*, 7502−7517.
(6) Gómez-Pacheco, C. V.; Sánchez-Polo, M.; Rivera-Utrilla, J.; López-Peñalver, J. Tetracycline removal from waters by integrated technologies based on ozonation and biodegradation. *Chem. Eng. J.* **2011**, *178*, 115−121.
(7) Guo, L.; Zhang, K.; Han, X.; Zhao, Q.; Wang, D.; Fu, F.; Liang, Y. Highly efficient visible-light-driven photo-Fenton catalytic performance over FeOOH/Bi_2WO_6 composite for organic pollutant degradation. *J. Alloys Compd.* **2020**, *816*, 152560.
(8) Duan, X.; Sun, H.; Shao, Z.; Wang, S. Nonradical reactions in environmental remediation processes: Uncertainty and challenges. *Appl. Catal., B* **2018**, *224*, 973−982.
(9) Cao, J.; Lai, L.; Lai, B.; Yao, G.; Chen, X.; Song, L. Degradation of tetracycline by peroxymonosulfate activated with zero-valent iron: Performance, intermediates, toxicity and mechanism. *Chem. Eng. J.* **2019**, *364*, 45−56.
(10) Wang, N.; Zheng, T.; Zhang, G.; Wang, P. A review on Fenton-like processes for organic wastewater treatment. *J. Environ. Chem. Eng.* **2016**, *4*, 762−787.
(11) Pirsaheb, M.; Moradi, S.; Shahlaei, M.; Wang, X.; Farhadian, N. Ultrasonic Enhanced Zero-Valent Iron-Based Fenton Reaction for Ciprofloxacin Removal under Aerobic Condition. *Environ. Processes* **2020**, *7*, 227−241.
(12) Pirsaheb, M.; Moradi, S.; Shahlaei, M.; Wang, X.; Farhadian, N. Simultaneously implement of both weak magnetic field and aeration for ciprofloxacin removal by Fenton-like reaction. *J. Environ. Manage.* **2019**, *246*, 776−784.
(13) Farhadian, N.; Liu, S.; Asadi, A.; Shahlaei, M.; Moradi, S. Enhanced heterogeneous Fenton oxidation of organic pollutant via Fe-containing mesoporous silica composites: A review. *J. Mol. Liq.* **2021**, *321*, 114896.
(14) Gao, Q.; Lin, D.; Fan, Y.; He, Q.; Wang, Q. Visible light induced photocatalytic reduction of Cr(VI) by self-assembled and amorphous Fe-2MI. *Chem. Eng. J.* **2019**, *374*, 10−19.
(15) Jin, H.; Tian, X.; Nie, Y.; Zhou, Z.; Yang, C.; Li, Y.; Lu, L. Oxygen Vacancy Promoted Heterogeneous Fenton-like Degradation of Ofloxacin at pH 3.2−9.0 by Cu Substituted Magnetic Fe_3O_4@FeOOH Nanocomposite. *Environ. Sci. Technol.* **2017**, *51*, 12699−12706.
(16) Wang, H.; Wang, C.; Cui, X.; Qin, L.; Ding, R.; Wang, L.; Liu, Z.; Zheng, Z.; Lv, B. Design and facile one-step synthesis of $FeWO_4$/Fe_2O_3 di-modified WO_3 with super high photocatalytic activity toward degradation of quasi-phenothiazine dyes. *Appl. Catal., B* **2018**, *221*, 169−178.
(17) Wang, X.; Zhang, X.; Zhang, Y.; Wang, Y.; Sun, S.-P.; Wu, W. D.; Wu, Z. Nanostructured semiconductor supported iron catalysts for heterogeneous photo-Fenton oxidation: a review. *J. Mater. Chem. A* **2020**, *8*, 15513.
(18) Zhang, X.; Zhang, Y.; Yu, Z.; Wei, X.; Wu, W. D.; Wang, X.; Wu, Z. Facile synthesis of mesoporous anatase/rutile/hematite triple heterojunctions for superior heterogeneous photo-Fenton catalysis. *Appl. Catal., B* **2020**, *263*, 118335.
(19) Ganiyu, S. O.; Zhou, M.; Martínez-Huitle, C. A. Heterogeneous electro-Fenton and photoelectro-Fenton processes: A critical review of fundamental principles and application for water/wastewater treatment. *Appl. Catal., B* **2018**, *235*, 103−129.
(20) Guo, Y.; Li, C.; Gong, Z.; Guo, Y.; Wang, X.; Gao, B.; Qin, W.; Wang, G. Photocatalytic decontamination of tetracycline and Cr(VI) by a novel α-FeOOH/FeS_2 photocatalyst: One-pot hydrothermal synthesis and Z-scheme reaction mechanism insight. *J. Hazard. Mater.* **2020**, *397*, 122580.
(21) Qian, X.; Ren, M.; Zhu, Y.; Yue, D.; Han, Y.; Jia, J.; Zhao, Y. Visible Light Assisted Heterogeneous Fenton-Like Degradation of Organic Pollutant via α-FeOOH/Mesoporous Carbon Composites. *Environ. Sci. Technol.* **2017**, *51*, 3993−4000.
(22) Qian, X.; Wu, Y.; Kan, M.; Fang, M.; Yue, D.; Zeng, J.; Zhao, Y. FeOOH quantum dots coupled g-C_3N_4 for visible light driving photo-Fenton degradation of organic pollutants. *Appl. Catal., B* **2018**, *237*, 513−520.
(23) Ma, Y.; Wang, B.; Wang, Q.; Xing, S. Facile synthesis of α-FeOOH/γ-Fe_2O_3 by a pH gradient method and the role of γ-Fe_2O_3 in H_2O_2 activation under visible light irradiation. *Chem. Eng. J.* **2018**, *354*, 75−84.
(24) Zeng, D.; Yang, K.; Yu, C.; Chen, F.; Li, X.; Wu, Z.; Liu, H. Phase transformation and microwave hydrothermal guided a novel double Z-scheme ternary vanadate heterojunction with highly efficient photocatalytic performance. *Appl. Catal., B* **2018**, *237*, 449−463.
(25) Hong, S. J.; Lee, S.; Jang, J. S.; Lee, J. S. Heterojunction $BiVO_4$/WO_3 electrodes for enhanced photoactivity of water oxidation. *Energy Environ. Sci.* **2011**, *4*, 1781.
(26) Liu, X.; Wang, J.; Dong, Y.; Li, H.; Xia, Y.; Wang, H. One-step synthesis of Bi_2MoO_6/reduced graphene oxide aerogel composite with enhanced adsorption and photocatalytic degradation performance for methylene blue. *Mater. Sci. Semicond. Process.* **2018**, *88*, 214−223.
(27) Hu, J.; Li, J.; Cui, J.; An, W.; Liu, L.; Liang, Y.; Cui, W. Surface oxygen vacancies enriched FeOOH/Bi_2MoO_6 photocatalysis-Fenton synergy degradation of organic pollutants. *J. Hazard. Mater.* **2020**, *384*, 121399.
(28) Hsueh, C. L.; Huang, Y. H.; Wang, C. C.; Chen, C. Y. Degradation of azo dyes using low iron concentration of Fenton and Fenton-like system. *Chemosphere* **2005**, *58*, 1409−1414.
(29) Zhao, Y.; Liang, X.; Wang, Y.; Shi, H.; Liu, E.; Fan, J.; Hu, X. Degradation and removal of Ceftriaxone sodium in aquatic environment with Bi_2WO_6/g-C_3N_4 photocatalyst. *J. Colloid Interface Sci.* **2018**, *523*, 7−17.
(30) Zhao, W.; Liang, C.; Wang, B.; Xing, S. Enhanced Photocatalytic and Fenton-like Performance of CuO_x-Decorated $ZnFe_2O_4$. *ACS Appl. Mater. Interfaces* **2017**, *9*, 41927−41936.
(31) Liu, C.; Lü, H.; Yu, C.; Ding, B.; Ye, R.; Ji, Y.; Dai, B.; Liu, W. Novel $FeWO_4$/WO_3 nanoplate with p-n heterostructure and its enhanced mechanism for organic pollutants removal under visible-light illumination. *J. Environ. Chem. Eng.* **2020**, *8*, 104044.
(32) Gao, Q.; Liu, Z. $FeWO_4$ nanorods with excellent UV−Visible light photocatalysis. *Prog. Nat. Sci.: Mater. Int.* **2017**, *27*, 556−560.
(33) Wang, J.; Zhi, D.; Zhou, H.; He, X.; Zhang, D. Evaluating tetracycline degradation pathway and intermediate toxicity during the electrochemical oxidation over a Ti/Ti_4O_7 anode. *Water Res.* **2018**, *137*, 324−334.
(34) Liu, M.; Hou, L.-a.; Xi, B.-d.; Li, Q.; Hu, X.; Yu, S. Magnetically separable Ag/AgCl-zero valent iron particles modified zeolite X heterogeneous photocatalysts for tetracycline degradation under visible light. *Chem. Eng. J.* **2016**, *302*, 475−484.

https://doi.org/10.1021/acsomega.1c00204
ACS Omega 2021, 6, 9095−9103